A Dual-Layer Ionosphere Model Based on 3-D Ionospheric Constraint

Hu Jiang, Shuanggen Jin, *Senior Member, IEEE*, Xingliang Huo, Hui Xi, Jiachun An, Jingbin Liu, Wengang Sang, and Qiuying Guo

***Abstract*— Traditional ionospheric models were mostly constructed based on a single-layer assumption from global navigation satellite system (GNSS) observations, while it cannot capture vertical information of the ionosphere. This study proposes a new method to construct a double-layer ionospheric model based on constraints from a 3-D ionospheric model, whereby the bottom and topside ionospheric total electron content (TEC) can be represented by two spherical harmonic (SH) functions. The new improved model allows two SH functions to capture the spatiotemporal TEC variations across the vertical range of the ionosphere. The determination of the two thin layer heights (TLHs) in the double-layer model is achieved through a minimum mapping function error. Moreover, the performance of the new model is validated using GPS, BDS, and Galileo data from the International GNSS Server (IGS) network and compared with the global ionospheric map (GIM). During the experiment period, the results indicate that: 1) the TLHs of the bottom and topside ionosphere exhibit distinct spatiotemporal trends with the optimal global heights as 350 and 650 km, respectively; 2) the average relative accuracies of the bottom and topside ionospheric models are up to 86.80% and 85.33%, respectively; 3) the new model demonstrates an improvement of approximately 20%–27% in terms of TEC when compared to the GIM model, with the rms better than 4.64, 2.99, and 3.61 TECU in the low, middle, and high latitudes, respectively; and 4) with the increase of geomagnetic activity, the performance of the double-layer model shows a slight decline, but its relative accuracy can still reach over 84.8%.**

***Index Terms*— Double-layer ionospheric model, global ionospheric map (GIM), global navigation satellite system (GNSS), total electron content (TEC), thin layer height (TLH).**

I. Introduction

THE ionosphere plays a crucial role in the solar-terrestrial space environment and has a close relationship with human activities. When the signal from the global navigation satellite system (GNSS) passes through the ionosphere, it undergoes reflection, refraction, and delay, resulting in group/phase delays ranging from a few meters to tens of meters [1], [2], [3]. For the majority of users who rely on single-frequency receivers, the ionospheric delay becomes the most significant and challenging error source in GNSS observations [4], [5], [6], [7]. Numerous studies have been conducted to mitigate the impact of ionospheric delay on GNSS navigation, positioning, and timing (PNT) by developing suitable ionospheric models [1], [8], [9].

The ionosphere model used to correct GNSS ionosphere delays includes the broadcast ionosphere model (such as the Klobuchar model used by GPS, the Klobuchar-like and BDGIM models used by BDS, and the NeQuick model used by Galileo), global ionospheric maps (GIMs) provided by the International GNSS Service (IGS), and grid-based ionospheric correction from a satellite-based augmentation system (SBAS) [10]. The broadcast ionosphere model only requires a few broadcast parameters to meet the ionospheric delay correction needs of many ordinary users during times of calm ionosphere [11], [12], [13]. However, for users who require high precision and security, the broadcast ionosphere model not only struggles to meet accuracy requirements but also lacks security guarantees during ionospheric storms [14], [15], [16]. To improve the accuracy and reliability of ionosphere error correction, the ionosphere model constructed based on GNSS measured total electron content (TEC) has been rapidly developed. Among them, the precise GIM released by Ionospheric Associated Analysis Centers (IAACs), such as Chinese Academy of Sciences (CAS), Wuhan University (WHU), and the Polytechnic University of Catalonia (UPC) within the context of the International GNSS Service (IGS)

Manuscript received 2 February 2024; revised 15 April 2024; accepted 26 May 2024. Date of publication 4 June 2024; date of current version 14 June 2024. This work was supported in part by the Shandong Provincial Natural Science Foundation under Grant ZR2022QD109, in part by the State Key Laboratory of Geodesy and Earth's Dynamics, Innovation Academy for Precision Measurement Science and Technology, CAS under Grant SKLGED2024-3-4, in part by the National Key Research and Development Program under Grant 2023YFA1009100, and in part by the National Natural Science Foundation of China under Grant 42230104 and Grant 42074045. *(Corresponding author: Jiachun An.)*

Hu Jiang is with the School of Surveying and Geo-Informatics, Shandong Jianzhu University, Jinan 250101, China, and also with the Key Laboratory of Polar Environment Monitoring and Public Governance (Wuhan University), Ministry of Education, Wuhan 430079, China (e-mail: jianghu21@sdjzu.edu.cn).

Shuanggen Jin is with the School of Surveying and Land Information Engineering, Henan Polytechnic University, Jiaozuo 454000, China, and also with the Shanghai Astronomical Observatory, Chinese Academy of Sciences, Shanghai 200030, China (e-mail: sgjin@shao.ac.cn).

Xingliang Huo is with the Innovation Academy for Precision Measurement Science and Technology, Chinese Academy of Sciences, Wuhan 430071, China (e-mail: xlhuo@whigg.ac.cn).

Hui Xi is with the College of Geography and Environment, Shandong Normal University, Jinan 250358, China (e-mail: xihui_sdnu@163.com).

Jiachun An is with Chinese Antarctic Center of Surveying and Mapping, Wuhan University, Wuhan 430079, China, and also with the Key Laboratory of Polar Environment Monitoring and Public Governance (Wuhan University), Ministry of Education, Wuhan 430079, China (e-mail: jcan@whu.edu.cn).

Jingbin Liu is with the State Key Laboratory of Information Engineering in Surveying, Mapping and Remote Sensing, Wuhan University, Wuhan 430079, China (e-mail: jingbin.liu@whu.edu.cn).

Wengang Sang and Qiuying Guo are with the School of Surveying and Geo-Informatics, Shandong Jianzhu University, Jinan 250101, China (e-mail: sang@sdjzu.edu.cn; qyguo@sdjzu.edu.cn).

Digital Object Identifier 10.1109/TGRS.2024.3409558

and International Association of Geodesy (IAG), has been widely used [17], [18].

The ionospheric models mentioned above are mainly single-layer ionospheric models. These models are widely used in GNSS applications due to their simplicity and ease of use. They also share a common assumption that the ionosphere may be horizontally stratified but spatially uniform [19], [20]. Furthermore, these models assume that all free electrons of the ionosphere are contained in a layer of infinitesimal thickness at a given reference altitude H. Although the single-layer model simplifies ionospheric TEC modeling and application, it may introduce mapping errors of more than ten TECUs [21], [22]. In order to accurately simulate the spatiotemporal changes of ionospheric electron density, many researchers have constructed ionospheric tomography models using multisource observation data [23], [24]. These models have been applied to electron density-related research. However, the data volume of the tomographic model is much higher than that of the thin-layer model, and the calculations are complex. As a result, it is difficult to use the tomographic model in satellite navigation.

In this case, numerous studies have attempted to simplify tomographic models by reducing spatial resolution and designing multilayer (more than two layers) ionospheric models [25], [26]. Shukla et al. [27] compared and analyzed the overall performance of the double-layer model and the multilayer model in the Indian region. The results showed that the accuracy of the double-layer model was superior to that of the multilayer model. Hernández-Pajares et al. [28] constructed a double-layer ionospheric model with a horizontal resolution of 5° (longitude) and 2.5° (latitude) using the kriging interpolation method based on carrier-phase observations. The distribution of ionospheric electron density within each individual cell is uniform. Compared to the single-layer ionospheric model, the GIM model established by UPC in Spain based on the double-layer approximation has improved the accuracy by 10%–20%. Li et al. [29] proposed constructing an ionospheric model based on the double-layer approximation and two spherical harmonic (SH) functions and conducted experiments in the Australian and Chinese regions, respectively. The results showed that the precision of the double-layer model can be improved by approximately 26% and 31% in the cross-validation experiment compared to the traditional single-layer model in the Australian and Chinese regions, respectively. However, Ren et al. [30] constructed a global double-layer ionospheric TEC model using SH functions based on simulated LEO constellations and ground-based GNSS data. The results revealed a decrease in the accuracy of the double-layer model compared to the single-layer model. We should note that when evaluating the efficacy of the double-layer model in improving ionosphere modeling, variations in statistical results may arise due to differences in experimental time, region selection, and comparison objects. Nevertheless, in general, the effectiveness of the double-layer model in global ionosphere modeling is inferior to that of regional models. Therefore, further research is needed on the global double-layer model. In addition, even though the double-layer approximation employs two SH functions to simulate the spatial and temporal changes of the bottom and topside ionospheric TEC, the ground-based GNSS-TEC data are not divided according to the designed range of the bottom and topside ionosphere during the modeling process. Consequently, the ionospheric TEC represented by the bottom and topside SH functions is tightly coupled together and fails to represent the changes of the bottom and topside ionosphere, respectively.

The thin-layer height (TLH) is an important parameter in the ionosphere model that affects the position of the ionospheric pierce point (IPP), mapping function, and the accuracy of ionosphere modeling [21], [31]. The commonly used ionospheric models determine the TLHs mainly based on experience. For example, the GPS Klobuchar, BDS Klobuchar, BDGIM, and GIM models use TLHs of 350, 375, 400, and 450 km, respectively [1], [12], [13]. In the case of the double-layer ionospheric model, Li et al. [32] developed a regional ionospheric model for China using bottom and topside TLHs of 300 and 750 km, respectively, while Shukla et al. [33] created an Indian regional ionospheric model using TLHs of 300 and 500 km. Hernández-Pajares et al. [34] constructed a global ionospheric model using TLHs of 450 and 1130 km. It should be noted that the TLH is influenced by ionospheric spatial gradients and changes over time, solar activity, latitude, and other factors [34]. Many studies have analyzed the variation characteristics of TLH under different ionospheric spatiotemporal states, as well as its impact on the accuracy of ionospheric models and DCB estimation [35], [36]. However, there has not been a systematic analysis of the TLH in the double-layer ionospheric model.

In this study, we propose a new double-layer ionospheric model based on SH functions and NeQuickG model constraints, which allows each group of SH functions to represent the TEC changes associated with the ionospheric range. Furthermore, we propose a method to detect the TLHs of the double-layer model using the theory of minimum mapping error. Finally, the global variation characteristics of the TLHs of the bottom and topside ionosphere are analyzed during the experimental stage. The performance of new double-layer model is validated and compared with the GIM model.

II. Data and Methodology

The new methodology is proposed to model the global TEC using GPS, BDS, and Galileo data from the IGS stations. The slant TEC data are extracted using the uncombined precise point positioning (UPPP) [37] based on the dual-frequency GNSS observations.

A. GNSS Observations

The test GNSS data (GPS, BDS, and Galileo data) provided by the International GNSS Server (IGS) were used in this study. The geographic distribution of the global stations selected in our experiment is shown in Fig. 1. The red dots represent the stations selected for developing the TEC model, while the green dots represent the verification stations used to verify the ionospheric TEC models. In total, there are 280 stations available, including 260 modeling stations and 20 validation stations. The GNSS measurements were taken

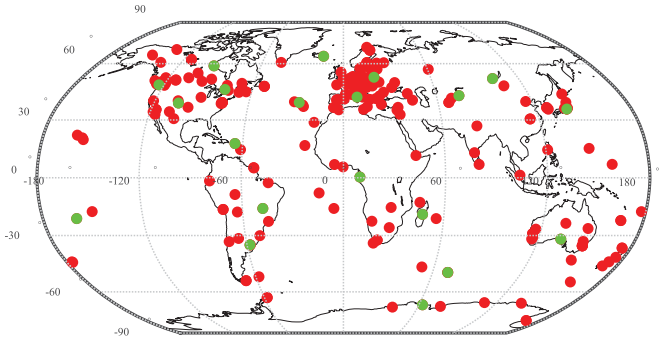

Fig. 1. Geographical locations of GNSS tracking stations from the International GNSS Service (IGS), including stations for modeling (red dots), and stations for validation (green dots).

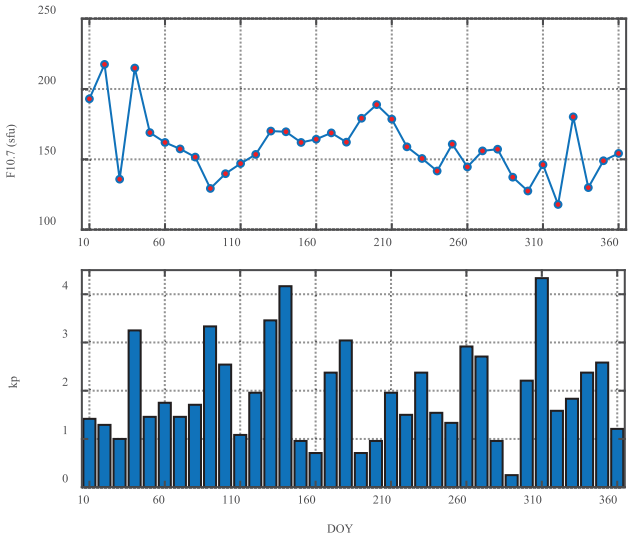

Fig. 2. Daily solar activity index F10.7 (top) and geomagnetic activity index kp (bottom) in 2023.

at a sampling rate of 30 s. To minimize the impact of spatial gradients and multipath effects on ionospheric mapping, only the observation data corresponding to the line-of-sight (LOS) with a cutoff angle of 20° were used at each observation point.

The ionosphere exhibits clear annual cyclic variations. In order to demonstrate a representative statistical result, we selected GNSS data spanning one year from the 10th day to 360th day in 2023 with a time interval of ten days to validate the performance of the new ionospheric model in this study. Fig. 2 shows the time series of the levels of solar activity, F10.7 (in standard flux unit, sfu), and geomagnetic activity, kp, for the year 2023 (https://omniweb.gsfc.nasa.gov/ow.html). To facilitate a more accessible and precise representation of the daily fluctuations in geomagnetic activity, we have determined the average kp index daily, employing a 3-hourly resolution for the kp values. It can be observed that the daily F10.7 index ranges from 120 to 220 sfu, and the kp index remains between 0.2 and 4.3. This indicates that the selected time is a high solar activity year, and the geomagnetic activity level covers from quiet to magnetic storm, which can be used to comprehensively verify the model performance.

B. Acquisition of Ionospheric Observables

According to the dispersion characteristics of the ionosphere on radio signals, the ionospheric delay of radio signals is a function of the signal frequencies, and the ionospheric TEC corresponds to the total number of electrons along a satellite-receiver path. The ionospheric observables can be derived from carrier-to-code leveling (CCL) and UPPP processes [37], [38]. The accuracy of ionospheric observables derived from the CCL approach relies on averaging the geometry-free linear combination within continuous arc segments, and the smoothing results are greatly affected by the continuous arc lengths and the noise level of code observables. Through reparametrization, UPPP can formulate full-rank function models. UPPP treats ionospheric observables as parameters to be estimated, fully utilizing precise satellite orbit and clock products as constraint information, thereby enhancing the robustness and reliability of ionospheric observation estimation. The accuracy of the UPPP-derived TEC can be improved by about 20%–40% in comparison with those from the CCL approach [37].

Therefore, the UPPP approach is used to derive the ionospheric TEC observations in this study. The ionospheric observable can be expressed as follows:

$$\hat{I}_{r,ik}^{j,s} = \mathrm{STEC}_r^{j,s} - \nu_{ik}^s \cdot \left(\mathrm{DCB}_{r,ik}^s + \mathrm{DCB}_{ik}^{j,s}\right) + \varepsilon_{\hat{I}} \quad (1)$$

where $\hat{I}_{r,ik}^{j,s}$ is the ionospheric observable in TEC unit (TECU); j, s, and r are the PRN of satellite, satellite system ($s = G$ for GPS, C for BDS, and E for Galileo), and the receiver, respectively; i and k denote frequencies $f_{s,i}$ and $f_{s,k}$ of GPS, BDS, or Galileo satellite carrier-phase observations (the GPS frequencies are $f_{G,1} = 1575.42$ MHz and $f_{G,2} = 1227.60$ MHz; the BDS frequencies are $f_{C,1} = 1561.098$ MHz and $f_{C,3} = 1268.52$ MHz; and the Galileo frequencies are $f_{E,1} = 1575.42$ MHz and $f_{\mathrm{E},2} = 1176.45$ MHz); $\nu = (c/\alpha(f_1^{-2} - f_2^{-2}))$ is a constant used to convert the time unit (second) to TECU, in which $\alpha = 40.28 \times 10^{16}$ ms^{-2}TECU^{-1} and c is the speed of light; $\mathrm{DCB}_{r,ik}^s$ and $\mathrm{DCB}_{ik}^{j,s}$ represent the receiver and satellite differential code bias (DCB), respectively; and $\varepsilon_{\hat{I}}$ denotes the noise level of the ionospheric observable.

C. Evaluation Indicators

In order to intuitively demonstrate the comprehensive performance of the ionospheric model, we compute the bias, rms error, the improvement level of the double-layer model relative to the single-layer model, and the relative correction accuracy (RMSrel) of the models regarding the GNSS-TEC in this study. The equations are shown as

$$\begin{cases} \mathrm{Bias} = \dfrac{1}{n}\displaystyle\sum_{i=1}^{n}\left(\mathrm{STEC}_{\mathrm{m}}^i - \mathrm{STEC}_r^i\right) \\ \mathrm{RMS} = \sqrt{\dfrac{1}{n}\displaystyle\sum_{i=1}^{n}\left(mf \cdot \mathrm{VTEC}_{\mathrm{m}}^i - \mathrm{STEC}_r^i\right)^2} \\ \mathrm{Improvement} = \dfrac{\mathrm{RMS_{DL}} - \mathrm{RMS_{SL}}}{\mathrm{RMS_{SL}}} \cdot 100\% \\ \mathrm{RMS_{rel}} = \left(1 - \mathrm{RMS}/\overline{\mathrm{STEC}_r}\right) \cdot 100\% \end{cases} \quad (2)$$

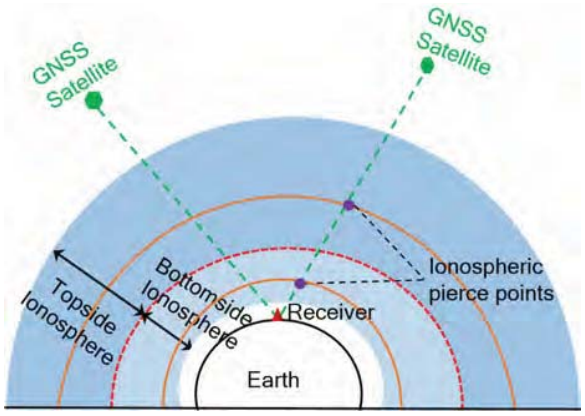

Fig. 3. Sketch map of the double-layer ionospheric model.

where n is the total number of samples; STEC_m^i and STEC_r^i denote the slant TEC from the ionospheric models and the reference TEC at the ith sample, respectively; $\mathrm{RMS}_{\mathrm{DL}}$ and $\mathrm{RMS}_{\mathrm{SL}}$ represent the rms errors of the double-layer model and single-layer model, respectively; *mf* represents the ionospheric mapping function; and $\overline{\mathrm{STEC}_r}$ is the mean value of reference TEC for used samples.

III. Double-Layer Ionospheric Model

In this section, we introduce the construction method of the double-layer model in detail and provide the determination method for the main parameter, which is the TLHs of the bottom and topside ionosphere. In addition, we will validate the performance of the new model by modeling the global TEC and comparing it with GIM.

A. Double-Layer Ionospheric Model Based on NeQuickG

As shown in Fig. 3, we divided the ionosphere into two parts in terms of vertical dimension: the topside and the bottom. The segmentation height (indicated by the red dashed line in the figure) of the topside and bottom parts is set to 500 km in this study. The height selection mainly considers the vertical variation characteristics of ionospheric electron density and minimizes the influence of ionospheric spatial gradient on the thin layer model as much as possible. Similar to the assumption in the single-layer ionospheric model, free electrons in the bottom and topside ionosphere are contained in two layers (represented by brown solid lines) with infinitesimal thickness at the reference altitudes H1 and H2, respectively. However, unlike the single-layer ionospheric model, when constructing and using the double-layer ionospheric model, the IPPs at the heights of the respective bottom and topside thin layers need to be calculated separately for each STEC measurement taken along the line of sight (LOS) from a GNSS satellite to a GNSS receiver. Therefore, under the assumption of the double-layer ionospheric model, each STEC measurement passes through two thin layers above and below, resulting in two IPPs. In this context, the conversion between the STEC and the VTEC utilizes a sine mapping function at the location of each IPP of the corresponding thin layer.

The bottom and topside ionospheric TEC can be expressed by

$$\mu_l \cdot \hat{I}_{r,ik}^{j,s} = mf(E,\ H_l) \cdot F_l(\phi_l, \lambda_l) + \mu_l \cdot v_{ik}^s \cdot \left(\mathrm{DCB}_{r,ik}^s + \mathrm{DCB}_{ik}^{j,s}\right) + \mu_l \cdot \varepsilon_r^s \tag{3}$$

where μ_l is the contribution to STEC from the lth (bottom or topside) layer; $mf(E, H_l) = 1/(1 - ((R \cdot \cos(E)/R + H_l))^2)^{1/2}$ is the mapping function used to convert the STEC to VTEC, which is a function of the satellite elevation (E) at the receiver and thin layer ionospheric height (H_l); and $F_l(\phi_l, \lambda_l)$ is a mathematical function used to simulate the spatiotemporal variation of the bottom or topside TEC.

The NeQuick model is a 3-D ionospheric model that can calculate the corresponding electron density based on input variables such as time, position, and solar activity indicators [39]. In order to overcome the dependency on solar activity, the Galileo broadcasting ionospheric model NeQuickG uses the effective ionization level Az as the driving parameter instead of the solar activity index [40]. Therefore, based on the propagation path of GNSS signals in the ionosphere, we can utilize the NeQuickG model [40] to calculate the topside and bottom ionospheric TECs of this path and obtain μ_l as follows:

$$\mu_l = \frac{\mathrm{STEC}_{l'}}{\mathrm{STEC}_r^{s'}} = \frac{\int_{L_l} N dL_l}{\int_L N dL} \tag{4}$$

where $\mathrm{STEC}_{l'}$ and $\mathrm{STEC}_r^{s'}$ represent the STEC in the line of sight direction of the lth layer and the entire ionosphere, respectively, which were calculated using the NeQuick model; and $N()$ represents the ionospheric electron density at any point. Compared to the prior method proposed by Li et al. [29], this constraint can effectively separate the topside and bottom ionospheres, enabling the double-layer ionospheric model to simulate the spatiotemporal changes of TEC in the topside and bottom ionospheres, respectively.

The SH function has an excellent mathematical structure for describing global changing physical quantities and has become one of the main functional models for modeling global ionospheric TEC. Therefore, the SH function is used to fit the global VTEC at each layer and is expressed as

$$F_l(\phi_l, \lambda_l) = \sum_{n=0}^{n_{\max}} \sum_{m=0}^{n} P_{nm}\left(\sin \varphi_{r,l}^s\right) \begin{pmatrix} A_{n,m,l} \cos\left(m \cdot \lambda_{r,l}^s\right) \\ +B_{n,m,l} \sin\left(m \cdot \lambda_{r,l}^s\right) \end{pmatrix} \tag{5}$$

where P_{nm} is the normalized Legendre function of degree n and order m; $n_{\max}$ is the maximum value of SH degree; ϕ_l and λ_l are the geographic latitude and Sun-fixed longitude of the IPP at the lth layer, respectively; and $A_{n,m,l}$ and $B_{n,m,l}$ are the SH coefficients to be estimated using GNSS data.

Furthermore, recognizing that ionospheric TEC variations are predominantly driven by solar activity, we model the ionospheric TEC against a solar-fixed frame. This approach allows for a smoother representation of spatial variations, enhancing the model's convenience and accuracy. Since the ionospheric TEC is closely tied to local time, we allocate

the 24-h calendar day into 12 equal sessions for comprehensive analysis. Based on the existing global ionospheric TEC modeling experience, the degree and order of the SH function at each layer are set to 15 ($n_{\max}$) [20]. For the receiver and satellite DCBs, we estimate them synchronously with the ionospheric model parameters as stable parameters within a day. The satellite DCBs cannot be distinguished from receiver DCB without introducing additional references. A zero-mean condition for all satellites suggested by the IGS [41] is adopted in this study. The model parameters for each session and the receiver and satellite DCBs are estimated using the least-squares method. The STEC measurements from different satellites and receivers are considered to be independent, and the variance of the STEC in the model estimation is calculated by

$$\sigma^2_{\mathrm{STEC}} = \psi(E)\sigma^2_{I_r^s} + \sigma^2_{\mathrm{DCB}^s} + \sigma^2_{\mathrm{DCB}_r} \tag{6}$$

where $\psi(E) = (1/\sin^2(E) + 1)$ is a function related to satellite elevation; $\sigma^2_{I_r^s}$ is the variance of the ionospheric delays estimated from the UPPP method; and $\sigma^2_{\mathrm{DCB}^s}$ and $\sigma^2_{\mathrm{DCB}_r}$ are the variance of the satellite and receiver DCBs, respectively.

B. Parameter Settings for the Double-Layer Ionospheric Model

The mean heights of the two thin layers in the regional double-layer ionospheric models are selected based on experience, resulting in differences due to the influence of spatial changes in the ionosphere. However, the TLHs of the globally applicable double-layer model have not been determined yet.

In this context, the principle for selecting the optimal TLH is to calculate the mapping function error (IME) of different TLHs and choose the TLHs that correspond to the minimum IME as the optimal TLH. This work used the NeQuickG model to calculate IME for various satellite elevations and azimuths. By taking the VTEC and STEC derived from the NeQuickG model as the reference, the mapping function errors at an IPP can be expressed as [21]

$$\begin{aligned}\mathrm{IME}&\left(\varphi_{\mathrm{ipp}},\ \lambda_{\mathrm{ipp}},\ E_i,\ A_j,\ H_k\right)\\ &= mf(E_i,\ H_k)\cdot\int_{s_1}^{s_2} N\left(\varphi_{\mathrm{ipp}},\ \lambda_{\mathrm{ipp}},\ E_i,\ A_j,\ s\right)\mathrm{d}s\\ &\quad - \int_{h_1}^{h_2} N\left(\varphi_{\mathrm{ipp}},\ \lambda_{\mathrm{ipp}},\ h\right)\mathrm{d}h\end{aligned} \tag{7}$$

where $(\varphi_{\mathrm{ipp}}, \lambda_{\mathrm{ipp}})$ is the geographical coordinates of the IPP; E_i and A_j are the elevation angle and azimuth angle, respectively; H_k is the TLH; $mf()$ refers to a mapping function that is identical to the one in (3); s_1 and s_2 represent the starting and ending points of the slant path of GNSS signal in the bottom or topside ionosphere, respectively; h_1 and h_2 represent the starting and ending points of the vertical path of GNSS signal in the bottom or topside ionosphere, respectively; and $\int_{s_1}^{s_2} N\left(\varphi_{\mathrm{ipp}},\ \lambda_{\mathrm{ipp}},\ E_i,\ A_j,\ s\right)\mathrm{d}s$ and $\int_{h_1}^{h_2} N\left(\varphi_{\mathrm{ipp}},\ \lambda_{\mathrm{ipp}},\ h\right)\mathrm{d}h$ are the VTEC and STEC through the same IPP, respectively.

As seen from (7), the IME at the IPP is only related to the TLH, the elevation angle, and the azimuth angle. By considering the elevations and azimuths of the IPP, we can evaluate the rms errors of the IMEs for different TLHs. As shown in (8), selecting the TLH that corresponds to the minimum rms error is the optimal TLH

$$\min\left(\mathrm{rms}\left(\mathrm{IME}\left(\varphi_{ipp,}\ \lambda_{\mathrm{ipp}},\ E_i,\ A_j,\ H_k\right)\right)\right) \rightarrow \mathrm{OTLIH} \tag{8}$$

where min() is a function that calculates the minimum value of a matrix and rms() is a function that calculates the rms error of a matrix.

On the global scale, 21 uniformly distributed GNSS observation stations were selected to calculate the optimal TLH based on (8) for both the bottom and topside ionospheres. In this experiment, the elevation and azimuth angles are equally spaced, with elevation angles ranging from 10° to 50° with one every 10° and azimuth angles ranging from 0° to 360° with one every 60°. In order to showcase the temporal and spatial variations of the TLH in different seasons, we have analyzed its most representative temporal and spatial changes around the spring equinox, summer solstice, autumn equinox, and winter solstice (DOY 80, 170, 270, and 360). Figs. 4 and 5 illustrate the optimal TLHs for the bottom and topside ionosphere at each GNSS station on DOY 80, 170, 270, and 360 of 2023. The resolutions of the TLH are set to 10 and 20 km for the topside and bottom ionosphere, respectively. For the bottom ionosphere, the optimal TLH typically varies from 220 to 400 km, with a decreasing trend as latitude increases. Conversely, for the topside ionosphere, the optimal TLH ranges from 550 to 850 km, exhibiting an upward trend as latitude increases. Clearly, due to the spatiotemporal variations in the ionosphere, the optimal TLH values vary over time and space. In different seasons, the TLH variation at the same station is small, with differences generally within a range of 50 km.

TABLE I
OPTIMAL TLHS OF BOTTOM AND TOPSIDE IONOSPHERE FOR THE DIFFERENT LATITUDES

Latitudinal band	TLH (km)	
	bottom	topside
0°~± 30°	380	600
± 30°~± 60°	325	660
± 60°~± 90°	275	880

In order to illustrate the relationship between TLH and latitude more intuitively, we calculated the optimal bottom and topside TLHs for different latitude bands based on IMEs using (7) in different seasons, as shown in Table I. As shown in the table, with the increase in latitude, the distance between the bottom and topside TLHs becomes increasingly larger. This indicates that as latitude increases, the electron density becomes more dispersed in the vertical direction. There are significant differences in the TLH of different latitude belts, especially between low and high latitudes.

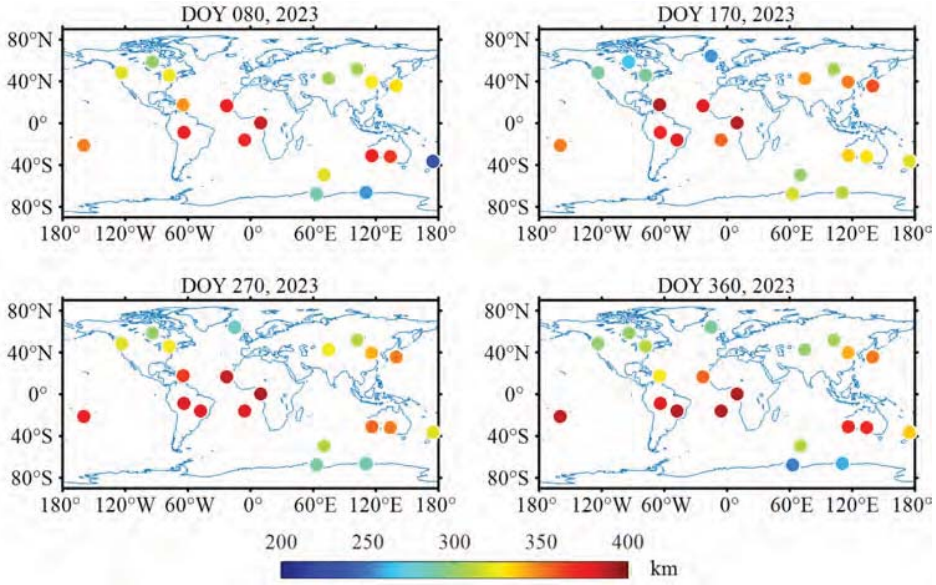

Fig. 4. Geographic distribution map concerning the bottom thin-layer height on DOY 80, 170, 270, and 360 in 2023.

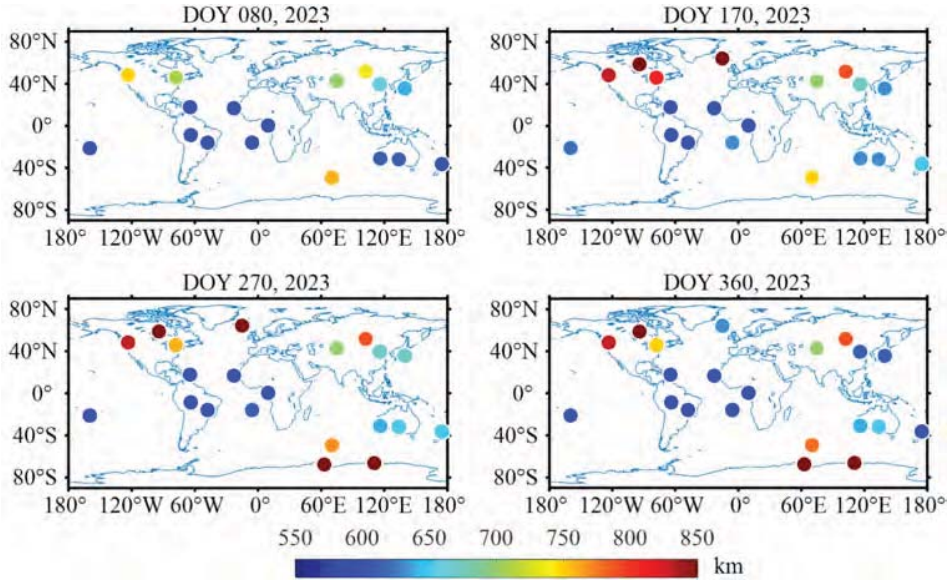

Fig. 5. Geographic distribution map concerning the top thin-layer height on DOY 80, 170, 270, and 360 in 2023.

However, to facilitate the construction and usage of a double-layer ionospheric model based on global observation data, we employed the aforementioned method to determine the optimal TLH values of 350 km for the bottom ionosphere and 650 km for the topside ionosphere during the experimental phase.

In addition, the ratio of bottom and topside ionospheric TECs is also a key parameter in the proposed model, as it affects the accuracy of each layer model. Fig. 6 presents the global spatial distribution of TEC ratios in the bottom and top ionosphere around the spring equinox, summer solstice, autumn equinox, and winter solstice in 2023 based on (4) using the NeQuickG model. According to the data used in this experiment, the ratio values range from 0.5 to 5.5. The ratio has a clear seasonal variation characteristic. At the vernal and autumnal equinoxes, the ratio is essentially symmetrical about the geomagnetic equator; the ratio in the hemisphere at summer solstice is significantly lower than that in the hemisphere at winter solstice. This phenomenon is closely related to the seasonal variations of the ionosphere caused by solar activity. Furthermore, the spatial distribution of ratio values varies at different times due to the influence of solar activity. On a global scale, the ratio between the bottom and topside ionospheric TEC is approximately 0.7:0.3.

IV. Performance of the TEC Models

A. Evaluation of Topside and Bottom Ionospheric Models

The first coefficient, representing the zero-order term of the SH function coefficients, indicates the average ionospheric

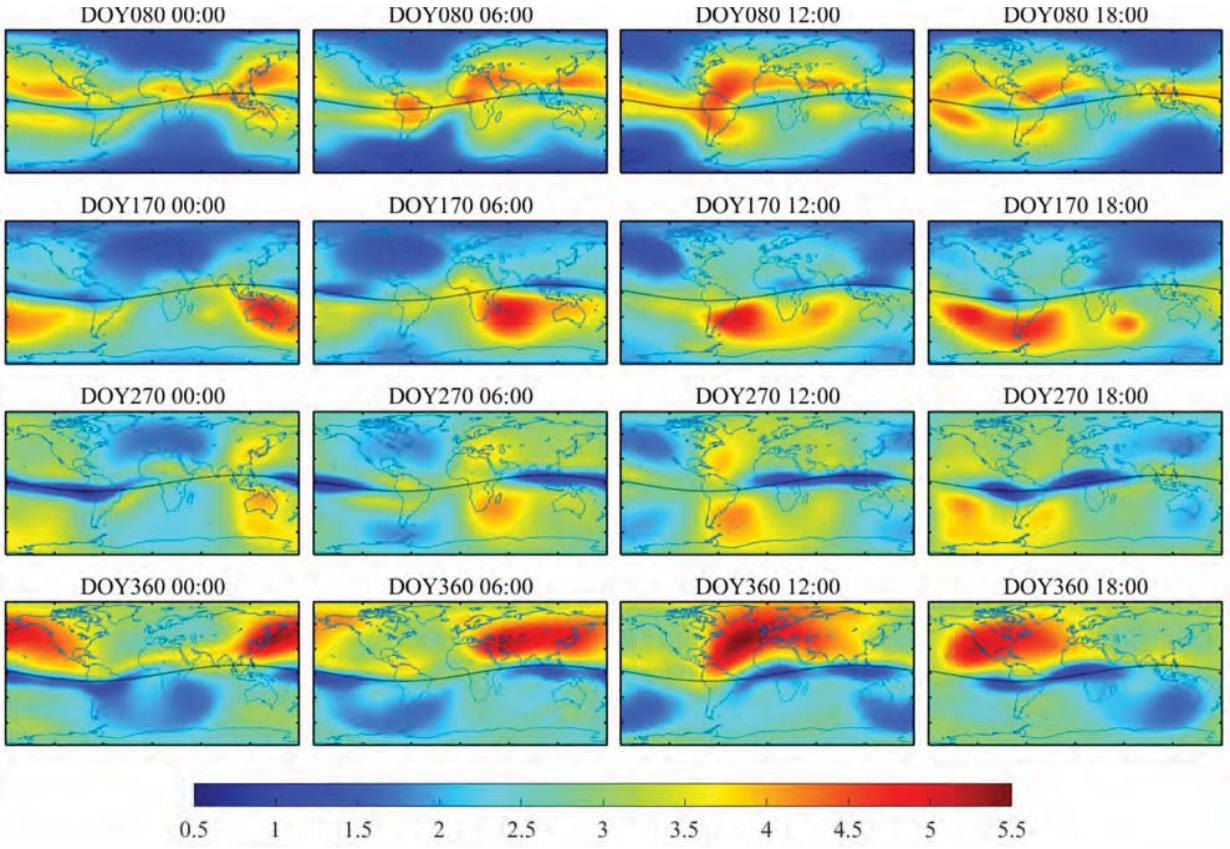

Fig. 6. Spatial distribution of TEC ratios in the bottom and top ionosphere of four seasons on DOY 80, 170, 270, and 360 in 2023.

TEC at each layer across the covered data area. The total of the first coefficients of the two SH functions gives the average global TEC value for each session. Fig. 7 shows the series of daily average ionospheric TEC of the first coefficients, including the bottom average TEC (represented by the green solid line) and the topside average TEC (represented by the blue solid line), as well as the sum of the two (represented by the red solid line). These are compared with the GIM model (represented by the black solid line). It can be observed that the series of the sum of the bottom and topside average TEC is very similar to that of the GIM model. The correlation coefficient between them is 0.97, with a bias of 1.60 TECU and rms errors of 2.03 TECU. In addition, the bottom and topside TEC series display a similar trend of change as the GIM-TEC. This reinforces the notion that the SH coefficients retain their physical relevance within the context of the proposed double-layer ionospheric model.

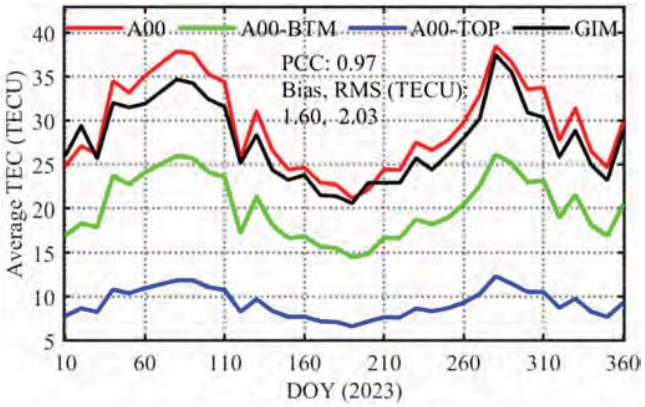

Fig. 7. Series of daily average ionospheric TEC directly extracted from the first coefficients of double-layer ionospheric model and GIM in global.

Figs. 8 and 9 show the spatial distributions of the bottom and topside ionospheric TEC at 13:00 UT during the four seasons (DOY 80, 170, 270, and 360) in 2023. As depicted in the figures, both the bottom and topside ionospheric TEC exhibit a bimodal structure on both sides of the equator. On a global scale, the TEC of the bottom ionosphere mainly ranges from 5 to 75 TECU, while the TEC of the topside ionosphere is generally between 2 and 35 TECU. In the same region, the TEC of the bottom ionosphere is approximately double that of the topside ionosphere. In addition, both the bottom and topside ionospheric models can not only demonstrate the distribution characteristics of the TEC in the ionosphere across the global range but also depict the subtle fluctuations of TEC in small areas. This also proves the performance of the model proposed in this study from a side view.

The disparity between the GNSS TEC measurements and the ionospheric model can indicate the consistency between the double-layer model and the actual observations. To assess the accuracy of both the bottom and topside ionospheric models, we divide the GNSS-TEC into two corresponding parts based on the proportional coefficient μ [as shown in (3)], which is calculated by the NeQuickG model.

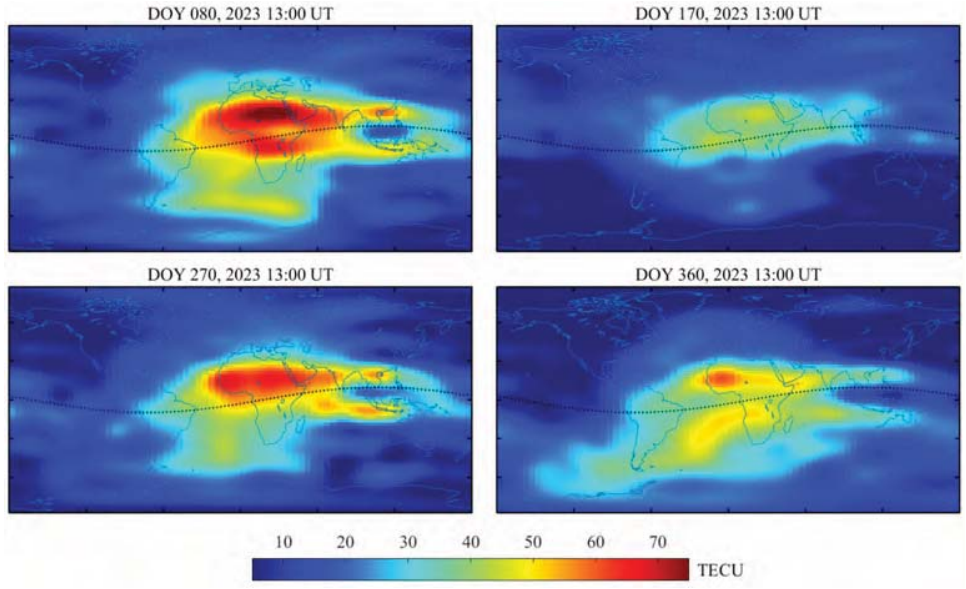

Fig. 8. Global maps of the bottom ionospheric TEC, referring to 13:00 UT on the DOY 080, 170, 270, and 360 of 2023.

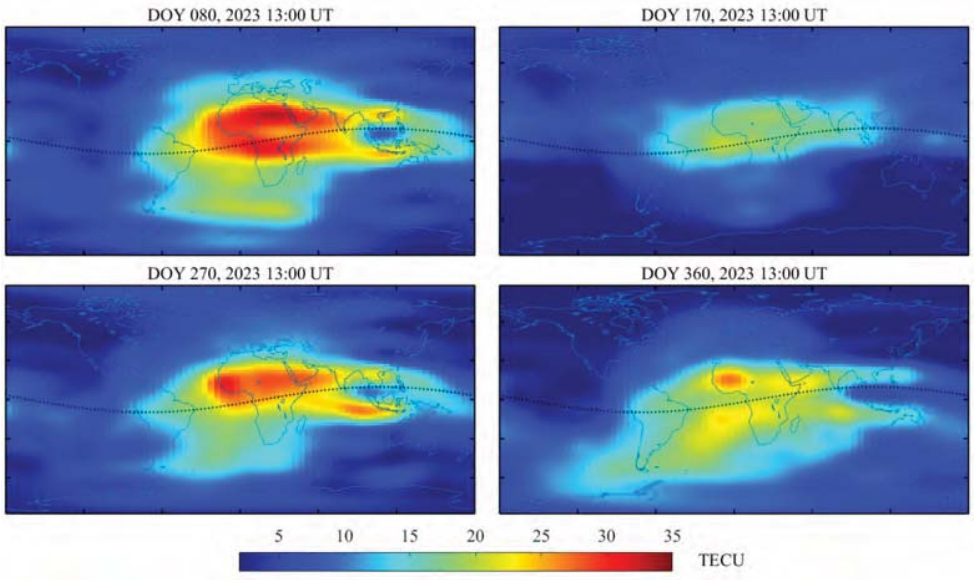

Fig. 9. Global maps of the top ionospheric TEC, referring to 13:00 UT on the DOY 080, 170, 270, and 360 of 2023.

Since the NeQuickG model is used in the modeling and the proportion coefficient μ has an uncertainty error, the evaluation result is provided only as a reference for the precision of internal coincidence. The normalized histograms of the errors (bias, rms, and relative rms errors) in the bottom and topside ionospheric models, relative to the GNSS TEC during DOYs 010 to 360 in 2023 with a sampling interval of ten days, are shown in Fig. 10. The data samples are the daily statistical values of each validation station, with a total of over 2100 samples. The bias of the bottom ionospheric model is mostly distributed between ± 4.5 TECU, while the bias of the topside model is mainly between ± 2.5 TECU. The majority of the rms errors of the bottom and topside ionospheric models are less than 6.0 and 3.0 TECU, respectively. In most cases, the correction accuracy of the bottom and topside ionospheric models is better than 60%. The topside ionospheric model exhibits lower bias and rms errors compared to the bottom ionospheric model. However, the relative accuracy of the bottom ionospheric model is higher than that of the topside ionospheric model. This is primarily because the TEC of the bottom ionosphere is higher than that of the topside ionosphere.

B. Comparison With GIM Model

In addition, the double-layer model is compared with the official IGSG-GIM product, which is derived through the collective weighting of GIM products provided by various ionospheric analysis centers of IGS. The IGSG-GIM model

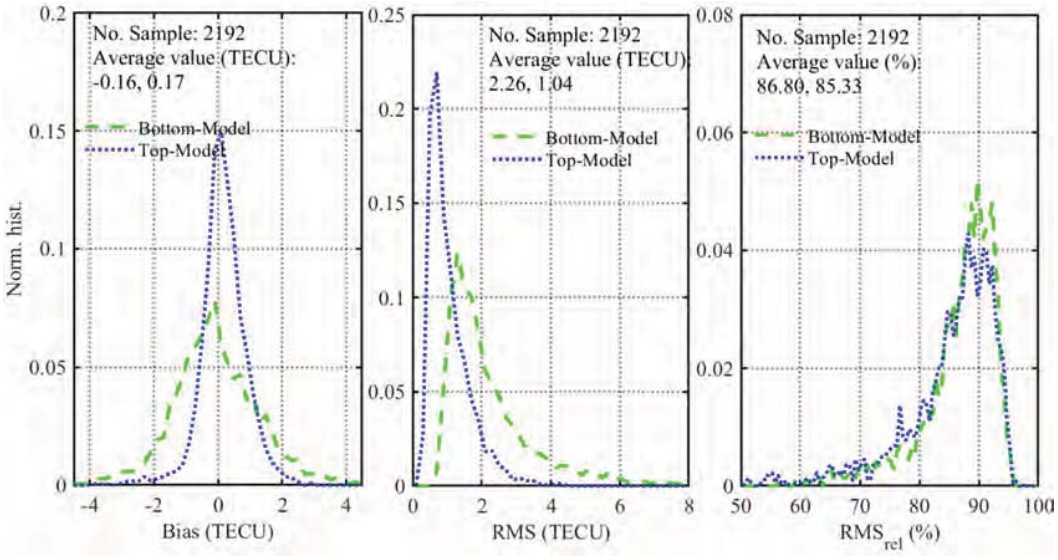

Fig. 10. Histograms of the bias, rms, and relative rms errors of bottom ionospheric model and top ionospheric model relative to GNSS TEC during the DOY 010–360 for the year 2023, with a sampling interval of ten days.

is renowned as one of the most precise global ionospheric TEC models available to the public, exhibiting a consistent bias of approximately 3.9 TECU and an rms error of roughly 4.2 TECU [16], [18]. Fig. 11 shows the spatial distribution of ionospheric TEC derived from the double-layer model and GIM at 13:00 UT during the four sections (DOYs 80, 170, 270, and 360) in 2023. As shown in the figure, the double-layer model and GIM exhibit similar overall characteristics in terms of TEC spatiotemporal distribution. From a more detailed perspective, the TEC distribution of the GIM model is smoother, while the double-layer model can accurately depict local TEC changes. This comparison indicates that the double-layer model has a significantly enhanced ability in capturing the spatial TEC variation. To better illustrate the differences between the double-layer model and GIM, the discrepancies between the two models were calculated, as shown in Fig. 12. The difference ranges from −20 to 15 TECU, with the largest disparity occurring in the polar and equatorial regions. In the ionospheric bimodal region near the geodetic equator, the TEC estimation of the double-layer model is lower than that of the GIM. On the contrary, the calculated values of the double-layer model in the polar regions are higher than those of the GIM, especially in the Antarctic region.

Furthermore, we conducted a comparative analysis of the bias, root-mean-square (rms) errors, and relative accuracy of the double-layer model against the GIM over the entire evaluation period, as depicted in Fig. 13. In order to simulate real-world conditions more accurately, we also assessed the model's capability in estimating STEC, an application where prediction errors are typically more substantial than those encountered in VTEC estimation. It can be observed that the double-layer model has better accuracy than GIM. Specifically, the biases of the double-layer model are mostly negative, while the biases of GIM are positive. This indicates that the double-layer model underestimates the ionospheric TEC, while GIM overestimated TEC in our experiment. It can also be found that the rms errors for double-layer model are much smaller, with a range of 2.5–4.5 TECU, compared to the GIM model's range of 3.5–5.8 TECU. Furthermore, the relative accuracy of the double-layer model is better than that of GIM, with the double-layer model achieving a relative accuracy ranging from 80% to 90%, while the GIM model achieved a relative accuracy between 76% and 85% during the test period.

Ionospheric changes have a close relationship with latitude. In order to analyze the comprehensive performance of the ionospheric model in different latitudes, we calculate the bias, rms, and relative accuracy of the double-layer model and GIM in high ($\pm 60^\circ \sim \pm 90^\circ$), middle ($\pm 30^\circ \sim \pm 60^\circ$), and low ($0^\circ \sim \pm 30^\circ$) latitudes, as shown in Table II. According to the table, the average bias of the double-layer model is approximately −0.49, −0.82, and −0.17 TECU during the entire test period in low, middle, and high latitudes, while it is approximately 4.49, 3.39, and 3.11 TECU for the GIM, respectively. Compared to the GIM model, the rms errors of the double-layer model are reduced by 1.22, 1.11, and 1.14 TECU in the low, middle, and high latitudes, respectively. The improvements of the double-layer model are about 20.8%, 27.1%, and 24.0% across the three latitude regions based on (2). The enhanced accuracy of the double-layer model is particularly noticeable in low and high latitudes, likely due to the heightened ionospheric activity in these regions. The model's ability to mitigate mapping errors arising from ionospheric spatial gradients is more pronounced in these areas. Moreover, at low latitudes, the impact of solar radiation on the ionosphere is more substantial, affecting its structure and density. Consequently, the double-layer ionospheric model can offer more precise predictions by capturing the intricate ionospheric conditions at these geographically distinct locations. Compared to the GIM model, the relative accuracy of the double-layer model improves by 4%, 5.1%, and 6.9% in the low-, medium-, and high-latitude regions, respectively. It can be seen that the relative accuracy in high-latitude areas has significantly decreased. The possible reason is that ionospheric debris and scintillation are more frequent in high-latitude

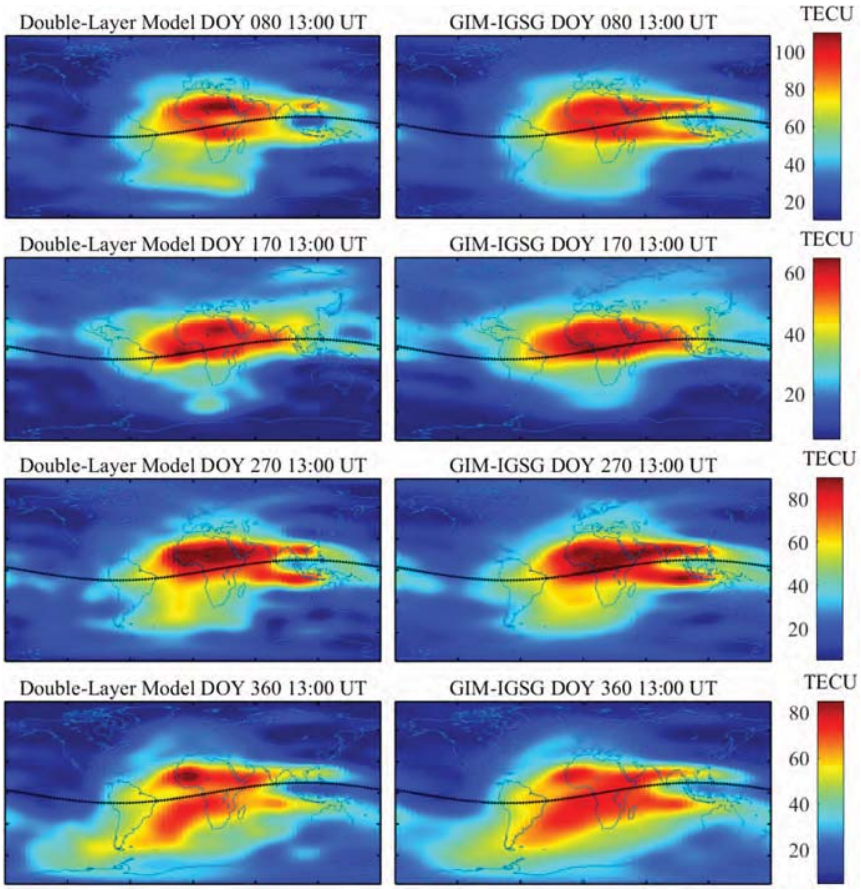

Fig. 11. Spatial distribution of mapping TEC of four sections derived from double-layer SH model (left) and GIM-IGSG (right) at 13:00 UT during DOY 80, 170, 270, and 360 in 2023.

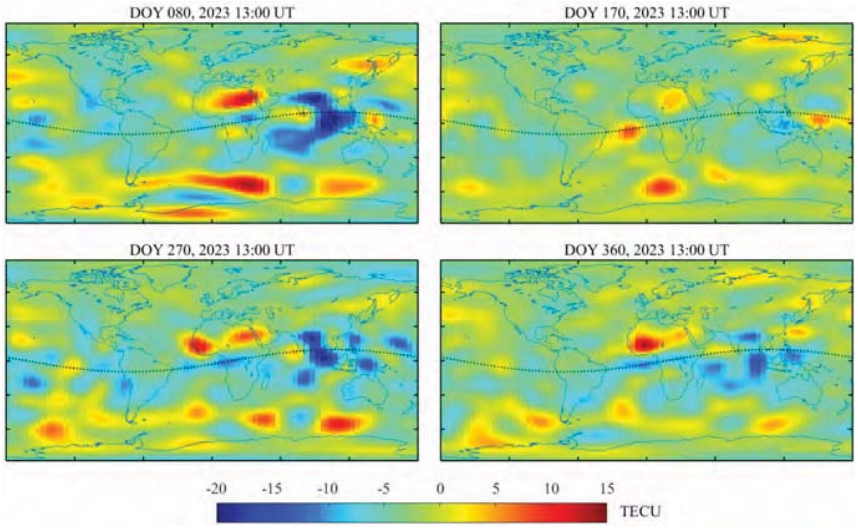

Fig. 12. Global maps of the TEC differences between double-layer ionospheric model and GIM-IGSG, referring to 13:00 UT during DOY 80, 170, 270, and 360 in 2023.

areas, resulting in a decrease in the quality of GNSS observation data. Furthermore, there is relatively little observational data available in the polar regions.

Geomagnetic activity is one of the main factors that affect the ionosphere. During intense geomagnetic activity, it can cause significant disturbances in the ionosphere, which in turn can impact the accuracy and reliability of TEC modeling. Therefore, it is necessary to analyze the performance of the double-layer model under different levels of geomagnetic activity. Table III provides information on the accuracy of both the GIM and double-layer models under three different levels of geomagnetic activity: quiet ($0 < \text{Kp} \leq 3$), unsettled ($3 < \text{Kp} \leq 4$), and active (above 4). It can be observed that there is a slight change in the deviation of the two models under

TABLE II

STATISTICAL RESULTS OF THE GIM AND DOUBLE-LAYER MODELS RELATIVE TO THE GNSS TEC VALUES IN THE DIFFERENT LATITUDE REGIONS IN 2023

Latitude band	Bias		RMS		RMS_{rel} (%)	
	GIM	DL	GIM	DL	GIM	DL
Low Lat.	4.49	-0.49	5.86	4.64	84.2	88.2
Mid. Lat.	3.19	-0.82	4.10	2.99	82.8	87.9
High Lat.	3.11	-0.17	4.75	3.61	72.5	79.4

The units of the bias and RMS are TECU

TABLE III

STATISTICAL RESULTS OF THE GIM AND DOUBLE-LAYER MODELS RELATIVE TO THE GNSS TEC VALUES UNDER DIFFERENT GEOMAGNETIC ACTIVITY CONDITIONS IN 2023

Geomagnetic activity (Kp)	Bias		RMS		RMS_{rel} (%)	
	GIM	DL	GIM	DL	GIM	DL
0-3 (Quiet)	3.37	-0.70	4.38	3.14	81.5	87.2
3-4 (Unsettled)	3.13	-0.68	4.22	3.30	81.0	85.8
>4 (Active)	3.41	-0.71	4.51	3.67	80.7	84.8

The units of the bias and RMS are TECU

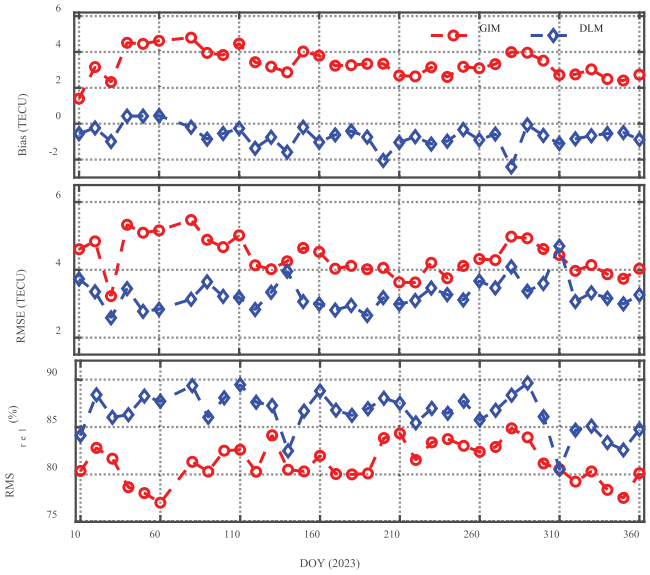

Fig. 13. Time series of the bias, rms, and relative accuracy for the GIM and double-layer model TEC estimates relative to the GNSS TEC in 2023.

different geomagnetic activity conditions. However, as the geomagnetic activity increases, the rms error of the dual-layer model increases and the relative correction accuracy decreases. Nevertheless, the dual-layer model still has certain advantages over the GIM model.

V. CONCLUSION

This study proposes a new method to construct a double-layer ionospheric model with constraints from the NeQuickG model. The TLH, an important parameter in the double-layer model, is determined based on the minimum mapping error method calculated from the NeQuick model. In addition, the performance of the proposed ionospheric model is comprehensively evaluated using GNSS TEC data and the GIM model under different seasons, latitudes, and geomagnetic activity. During the experiment period, the results show that the optimal TLH of the bottom ionosphere typically ranges from 220 to 400 km, with a decreasing trend as latitude increases. Conversely, for the topside ionosphere, the optimal TLH varies between 550 and 850 km, with an upward trend as latitude increases. Taking into account different seasons and latitudes, the optimal TLHs globally are 350 and 650 km in the bottom and topside ionosphere, respectively. Regarding the proposed ionospheric model, our test results demonstrate the following: 1) the SH coefficients still hold physical meanings in the double-layer model, with a correlation coefficient of 0.97 between the first coefficient of the double-layer model and the GIM; 2) the average relative accuracies of the bottom and topside ionospheric models are 86.80% and 85.33%, respectively; 3) the performance of the new model derived TEC is improved by approximately 20%–27%, and rms errors in the low, middle, and high latitudes are generally better than 4.64, 2.99, and 3.61 TECU, respectively, when compared to the GIM model; and 4) with the increase of geomagnetic activity, the performance of the double-layer model shows a slight decline, but its relative accuracy can still reach over 84.8%.

It should be noted that: 1) the TLHs used in this study are only applicable to the corresponding bottom and topside

ionospheric ranges; 2) further analysis is needed on the performance of the SH function for each layer; and 3) the evaluation results of the model's performance are limited to representing the high solar activity year of 2023. In the future, we will further focus on comprehensively analyzing the performance of the double-layer model in different ionospheric regions, levels of solar activity, and each layer model.

ACKNOWLEDGMENT

The authors would like to acknowledge the International GNSS Services (IGS) for providing access to the GNSS observations.

REFERENCES

[1] M. Hernández-Pajares et al., "The ionosphere: Effects, GPS modeling and the benefits for space geodetic techniques," *J. Geodesy*, vol. 85, no. 12, pp. 887–907, Dec. 2011.

[2] S. Jin, Q. Wang, and G. Dardanelli, "A review on multi-GNSS for Earth observation and emerging applications," *Remote Sens.*, vol. 14, no. 16, p. 3930, Aug. 2022.

[3] K. Su, S. Jin, and M. Hoque, "Evaluation of ionospheric delay effects on multi-GNSS positioning performance," *Remote Sens.*, vol. 11, no. 2, p. 171, Jan. 2019.

[4] R. Warnant, "Mitigation of ionospheric effects on GNSS," *Ann Geophys.*, vol. 52, nos. 3–4, pp. 373–390, Sep. 2010.

[5] J. Liu, R. Chen, Z. Wang, and H. Zhang, "Spherical cap harmonic model for mapping and predicting regional TEC," *GPS Solutions*, vol. 15, no. 2, pp. 109–119, Apr. 2011.

[6] D. J. Allain and C. N. Mitchell, "Ionospheric delay corrections for single-frequency GPS receivers over Europe using tomographic mapping," *GPS Solutions*, vol. 13, no. 2, pp. 141–151, Nov. 2008.

[7] S. Jin and J.-U. Park, "GPS ionospheric tomography: A comparison with the IRI-2001 model over South Korea," *Earth, Planets Space*, vol. 59, no. 4, pp. 287–292, May 2007.

[8] T. Dao et al., "Regional ionospheric corrections for high accuracy GNSS positioning," *Remote Sens.*, vol. 14, no. 10, p. 2463, May 2022.

[9] A.-L. Tao and S.-S. Jan, "Wide-area ionospheric delay model for GNSS users in middle- and low-magnetic-latitude regions," *GPS Solutions*, vol. 20, no. 1, pp. 9–21, Jan. 2016.

[10] J. Arenas, E. Sardón, A. Sainz, B. Ochoa, and S. Magdaleno, "Low-latitude ionospheric effects on SBAS," *Radio Sci.*, vol. 51, no. 6, pp. 603–618, Jun. 2016.

[11] B. Bidaine and R. Warnant, "Ionosphere modelling for Galileo single frequency users: Illustration of the combination of the NeQuick model and GNSS data ingestion," *Adv. Space Res.*, vol. 47, no. 2, pp. 312–322, Jan. 2011.

[12] J. A. Klobuchar, "Ionospheric time-delay algorithm for single-frequency GPS users," *IEEE Trans. Aerosp. Electron. Syst.*, vol. AES-23, no. 3, pp. 325–331, May 1987.

[13] Y. Yuan, N. Wang, Z. Li, and X. Huo, "The BeiDou global broadcast ionospheric delay correction model (BDGIM) and its preliminary performance evaluation results," *Navigation*, vol. 66, no. 1, pp. 55–69, Jan. 2019.

[14] S. Basu et al., "Ionospheric effects of major magnetic storms during the international space weather period of September and October 1999: GPS observations, VHF/UHF scintillations, and in situ density structures at middle and equatorial latitudes," *J. Geophys. Res., Space Phys.*, vol. 106, no. A12, pp. 30389–30413, Dec. 2001.

[15] P. V. S. R. Rao, S. Gopi Krishna, J. V. Prasad, S. N. V. S. Prasad, D. S. V. D. Prasad, and K. Niranjan, "Geomagnetic storm effects on GPS based navigation," *Annales Geophys.*, vol. 27, no. 5, pp. 2101–2110, May 2009.

[16] H. Jiang et al., "Assessment of spatial and temporal TEC variations derived from ionospheric models over the polar regions," *J. Geodesy*, vol. 93, no. 4, pp. 455–471, Apr. 2019.

[17] A. García-Rigo et al., "Global prediction of the vertical total electron content of the ionosphere based on GPS data," *Radio Sci.*, vol. 46, no. 6, pp. 1–3, Dec. 2011.

[18] D. Roma-Dollase et al., "Consistency of seven different GNSS global ionospheric mapping techniques during one solar cycle," *J. Geodesy*, vol. 92, no. 6, pp. 691–706, Jun. 2018.

[19] Y. Memarzadeh, "Ionospheric modeling for precise GNSS applications," Ph.D. dissertation, Delft Inst. Earth Observ. Space Syst., Delft Univ. Technology, Delft, The Nederlands, 2009.

[20] S. Schaer, "Mapping and predicting the Earth's ionosphere using the Global Positioning System," Ph.D. dissertation, Astronomical Inst. Univ. Bern, Bern, Switzerland, 1999.

[21] H. Jiang, Z. Wang, J. An, J. Liu, N. Wang, and H. Li, "Influence of spatial gradients on ionospheric mapping using thin layer models," *GPS Solutions*, vol. 22, no. 1, p. 2, Jan. 2018.

[22] B. Nava, S. M. Radicella, R. Leitinger, and P. Coïsson, "Use of total electron content data to analyze ionosphere electron density gradients," *Adv. Space Res.*, vol. 39, no. 8, pp. 1292–1297, Jan. 2007.

[23] B. Chen, L. Wu, W. Dai, X. Luo, and Y. Xu, "A new parameterized approach for ionospheric tomography," *GPS Solutions*, vol. 23, no. 4, pp. 96–111, Oct. 2019.

[24] D. Wen, Y. Wang, and R. Norman, "A new two-step algorithm for ionospheric tomography solution," *GPS Solutions*, vol. 16, no. 1, pp. 89–94, Jan. 2012.

[25] Y. Sui et al., "Multilayer ionospheric model constrained by physical prior based on GNSS stations," *IEEE J. Sel. Topics Appl. Earth Observ. Remote Sens.*, vol. 16, pp. 1842–1857, 2023.

[26] S. Gu et al., "Quasi-4-dimension ionospheric modeling and its application in PPP," *Satell. Navigat.*, vol. 3, no. 1, p. 24, Nov. 2022.

[27] A. K. Shukla, M. R. Sivaraman, and K. Bandyopadhyay, "A comparison study of voxel based multi- and two-layer ionospheric tomography models over the Indian region using GPS data," *Int. J. Remote Sens.*, vol. 31, no. 10, pp. 2535–2549, May 2010.

[28] M. Hernández-Pajares, J. M. Juan, and J. Sanz, "New approaches in global ionospheric determination using ground GPS data," *J. Atmos. Solar-Terr. Phys.*, vol. 61, no. 16, pp. 1237–1247, Nov. 1999.

[29] Z. Li, N. Wang, L. Wang, A. Liu, H. Yuan, and K. Zhang, "Regional ionospheric TEC modeling based on a two-layer spherical harmonic approximation for real-time single-frequency PPP," *J. Geodesy*, vol. 93, no. 9, pp. 1659–1671, Sep. 2019.

[30] X. Ren, J. Zhang, J. Chen, and X. Zhang, "Global ionospheric modeling using multi-GNSS and upcoming LEO constellations: Two methods and comparison," *IEEE Trans. Geosci. Remote Sens.*, vol. 60, 2022, Art. no. 5800215.

[31] D. A. Smith, E. A. Araujo-Pradere, C. Minter, and T. Fuller-Rowell, "A comprehensive evaluation of the errors inherent in the use of a two-dimensional shell for modeling the ionosphere," *Radio Sci.*, vol. 43, no. 6, pp. 1–23, Dec. 2008.

[32] M. Li et al., "Determination of the optimized single-layer ionospheric height for electron content measurements over China," *J. Geodesy*, vol. 92, no. 10, pp. 169–183, 2018.

[33] A. K. Shukla, S. Das, N. Nagori, M. R. Sivaraman, and K. Bandyopadhyay, "Two-shell ionospheric model for Indian region: A novel approach," *IEEE Trans. Geosci. Remote Sens.*, vol. 47, no. 8, pp. 2407–2412, Aug. 2009.

[34] M. Hernández-Pajares et al., "Polar electron content from GPS data-based global ionospheric maps: Assessment, case studies, and climatology," *J. Geophys. Res., Space Phys.*, vol. 125, no. 6, Jun. 2020, Art. no. e2019JA027677.

[35] H. Jiang et al., "A new method to determine the optimal thin layer ionospheric height and its application in the polar regions," *Remote Sens.*, vol. 13, no. 13, p. 2458, Jun. 2021.

[36] Y. Xiang and Y. Gao, "An enhanced mapping function with ionospheric varying height," *Remote Sens.*, vol. 11, no. 12, p. 1497, Jun. 2019.

[37] B. Zhang, "Three methods to retrieve slant total electron content measurements from ground-based GPS receivers and performance assessment," *Radio Sci.*, vol. 51, no. 7, pp. 972–988, Jul. 2016.

[38] A. J. Mannucci, B. D. Wilson, D. N. Yuan, C. H. Ho, U. J. Lindqwister, and T. F. Runge, "A global mapping technique for GPS-derived ionospheric total electron content measurements," *Radio Sci.*, vol. 33, no. 3, pp. 565–582, May 1998.

[39] G. Di Giovanni and S. M. Radicella, "An analytical model of the electron density profile in the ionosphere," *Adv. Space Res.*, vol. 10, no. 11, pp. 27–30, Jan. 1990.

[40] M. M. Hoque and N. Jakowski, "An alternative ionospheric correction model for global navigation satellite systems," *J. Geodesy*, vol. 89, no. 4, pp. 391–406, Apr. 2015.

[41] J. Feltens and S. Schaer, "IGS products for the ionosphere," in *Proc. IGS Anal. Centers Workshop*, Feb. 1998, pp. 225–232.

Hu Jiang received the M.S. degree in surveying engineering from the University of Chinese Academy of Sciences, Beijing, China, in 2016, and the Ph.D. degree in geodesy and survey engineering from Wuhan University, Wuhan, China, in 2019.

He is currently a Lecturer with the School of Surveying and Geo-Informatics, Shandong Jianzhu University, Jinan, China. His research interests include ionospheric modeling and GNSS precise point positioning.

Shuanggen Jin (Senior Member, IEEE) was born in Anhui, China, in 1974. He received the B.Sc. degree in geodesy from Wuhan University, Wuhan, China, in 1999, and the Ph.D. degree in geodesy from the University of Chinese Academy of Sciences, Beijing, China, in 2003.

He is currently the Vice President and a Professor with Henan Polytechnic University, Jiaozuo, China, and a Professor with Shanghai Astronomical Observatory, Chinese Academy of Sciences (CAS), Shanghai, China. He has over 500 articles in peer-reviewed journals and proceedings, ten patents/software copyrights, and ten books/monographs with more than 12 000 citations, and H-index is >60. His main research areas include satellite navigation, remote sensing, space geodesy, and space/planetary exploration.

Prof. Jin was the President of the International Association of Planetary Sciences (IAPS) from 2013 to 2017 and the International Association of CPGPS from 2016 to 2017, the Chair of IUGG Union Commission on Planetary Sciences (UCPS) from 2015 to 2023, the Vice President of the IAG Commission 2 from 2015 to 2019, the Vice Chair of COSPAR's Panel on Satellite Dynamics (PSD) from 2016 to 2020, and the Advances in Space Research from 2013 to 2017. He has been the Editor-in-Chief of the *International Journal of Geosciences* since 2010, an Associate Editor of IEEE TRANSACTIONS ON GEOSCIENCE AND REMOTE SENSING since 2014 and the *Journal of Navigation* since 2014, and an Editorial Board Member of the *GPS Solutions* since 2016, the *Journal of Geodynamics* since 2014, and the *Planetary and Space Science* since 2014. He has received one first-class and four second-class prizes of provincial awards; the 100-Talent Program of CAS in 2010; a fellow of IAG in 2011; the Fu Chengyi Youth Science and Technology Award in 2012; the Xia Jianbai Award of Geomatics in 2014; a member of the Russian Academy of Natural Sciences in 2017 and the European Academy of Sciences in 2018; an IUGG Fellow in 2019; a member of Academia Europaea in 2019 and the Turkish Academy of Sciences in 2020; the World Class Professor of Ministry of Education and Cultures, Indonesia, in 2021; and a fellow of the Electromagnetics Academy, USA, in 2021.

Xingliang Huo was born in Pingyao, Shanxi, China, in 1978. He received the B.Sc. degree in surveying engineering from Chang'an University, Xi'an, China, in 2001, and the Ph.D. degree in geodesy and surveying engineering from the Institute of Geodesy and Geophysics, Chinese Academy of Sciences, Beijing, China, in 2009.

He is currently a Professor with the Innovation Academy of Precision Measurement Science and Technology, Chinese Academy of Sciences. His research focuses on the inversion of the high-precise total electron content (TEC) and ionospheric electron density (IED) using GNSS data, and the effects of ionosphere weather on GNSS navigation and positioning.

Hui Xi received the B.S. degree in surveying engineering from the Shandong University of Technology, Zibo, China, in 2013, and the Ph.D. degree from the Institute of Geodesy and Geophysics, CAS, in 2019.

She is currently a Lecturer with the College of Geography and Environment, Shandong Normal University, Jinan, China. Her research interests are GNSS positioning and climate change.

Jiachun An was born in Bengbu, Anhui, China, in 1985. He received the B.S. degree in surveying engineering from Southeast University, Nanjing, China, in 2006, and the Ph.D. degree in geodesy and surveying engineering from Wuhan University, Wuhan, China, in 2011.

He was a Visiting Scholar with the Universitat Politècnica de Catalunya, Barcelona, Spain, from 2017 to 2018. He is currently an Associate Professor with Chinese Antarctic Center of Surveying and Mapping, Wuhan University. He has authored two books and more than 50 articles. His research interests include global navigation satellite system (GNSS) positioning, reflectometry, remote sensing, and applications over polar regions.

Dr. An was a recipient of the Luojia Young Scholar Award in 2017.

Jingbin Liu received the M.Sc. and Ph.D. degrees in geodesy and geomatics from Wuhan University, Wuhan, China, in 2004 and 2008, respectively.

He is currently a Professor in positioning and navigation with the State Key Laboratory of Information Engineering in Surveying, Mapping and Remote Sensing (LIESMARS), Wuhan University. He worked as a Specialist Research Scientist with the Finnish Geospatial Research Institute (FGI, formerly known as Finnish Geodetic Institute), Masala, Finland, from 2008 to 2016. His research interests include GNSS positioning, GNSS-based ionosphere mapping, and geospatial AI applications.

Wengang Sang received the M.Sc. and Ph.D. degrees in geodesy and geomatics from Hohai University, Nanjing, China, in 2001 and 2008, respectively.

He is currently a Professor with the College of Surveying and Geo-Informatics, Shandong Jianzhu University, Jinan, China. His study interests include satellite precision navigation and positioning and its applications in deformation for high-rise slope and building, GNSS-R, and 3-D modeling using laser scanners and vision.

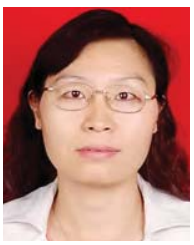

Qiuying Guo received the Ph.D. degree from China University of Mining and Technology (Beijing), Beijing, China, in 2008.

She is currently a Professor with the College of Surveying and Geo-Informatics, Shandong Jianzhu University, Jinan, China. Her research involves GNSS precise point positioning and GNSS meteorology.